arXiv:2512.06179v3 [cs.CV] 1 Jul 2026

Cast and Attached Shadow Detection via Iterative Light and Geometry Reasoning

Shilin Hu[1], Jingyi Xu[1], Sagnik Das[1], Dimitris Samaras[1†], and Hieu Le[2†]

[1] Stony Brook University, Stony Brook NY 11794, USA
[2] UNC Charlotte, Charlotte NC 28223, USA
{shilhu,jingyixu,sadas,samaras}@cs.stonybrook.edu, hle40@charlotte.edu

Abstract. Shadows encode rich information about scene geometry and illumination, yet existing methods either predict a unified shadow mask or overlook attached shadows entirely. We address this gap by proposing a framework for jointly detecting cast and attached shadows through explicit physical modeling of light direction and surface geometry under a dominant directional-light setting. Our approach is grounded in a simple observation: surfaces facing away from the light source tend to fall into shadow. We exploit the reciprocal relationship between shadow formation and light estimation to construct a closed feedback loop, a dual-module architecture in which a shadow detection module and a light estimation module iteratively refine each other. At each pass, updated light estimates, together with surface normals, produce partial attached shadow maps that guide detection, while improved shadow predictions sharpen light estimation. To support training and evaluation, we introduce a dataset of 1,458 images with manually annotated cast and attached shadow masks sourced from three existing benchmarks. Experiments demonstrate that our proposed method outperforms prior methods, with at least a 33% reduction in attached-shadow BER, while maintaining strong full-shadow and cast-shadow performance. Project page: https://shilin21.github.io/attached_detection/

Keywords: Shadow detection · Attached shadow

1 Introduction

Shadows define how we perceive shape, depth, and illumination in visual scenes. They are commonly categorized into two types: cast shadows, which appear on external surfaces and reveal spatial relations between objects [19, 31, 35, 47], and attached shadows, which form directly on an object's surface when light is blocked due to the surface's geometry and orientation relative to the light source [17, 78]. Together, these two shadow types encode complementary cues about scene structure and illumination, enriching visual realism and 3D perception [5, 58, 70, 72].

† Equal advising.

Table 1: Comparison of recent shadow detection datasets. Most existing datasets omit attached shadows or annotate them only implicitly, while our dataset provides explicit cast/attached shadow annotations as separate classes.

Dataset	Att.	#Imgs	Split
SBU [51]	✓ (occ.)	4.1K	✗
ISTD [52]	✗	1.9K	✗
SOBA [55]	✗	1.0K	✗
ViSha [3]	✗	11.7K	✗
SILT [67]	✓	0.6K	✗
CUHK [14]	✓	10.5K	✗
Ours	✓	1.5K	✓



Input Unified Mask Separate Masks

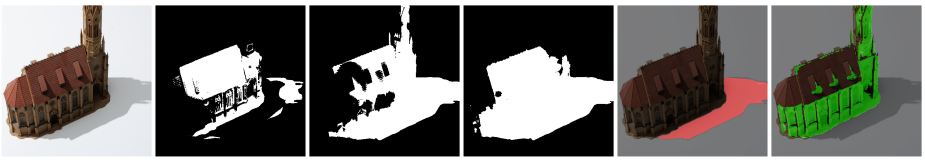
Fig. 1: Effect of shadow mask granularity on removal quality. Using a unified shadow mask, ShadowFormer [10] over-attenuates object regions. Using separate cast and attached shadow masks sequentially enables targeted correction and recovers natural object color.

However, most modern shadow detection methods predict a unified shadow mask [14,51,67], or ignore attached shadows entirely [3,52,55] (see Tab. 1). As a result, **explicitly** modeling attached shadows remains largely unexplored in the literature, despite their potential usefulness in downstream applications. In 3D shape reconstruction, attached shadows provide strong cues about local surface orientation and therefore reveal valuable information about the underlying geometry of objects. In shadow removal, separate cast and attached masks enable more targeted correction of receiving surfaces and object regions. As a simple illustration, applying an existing method [10] with separate cast and attached masks improves removal quality over using a single unified mask (see Fig. 1).

Yet attached shadow detection is far more than a simple extension of existing shadow detection approaches. As we will show experimentally, naive adaptations of current methods [4, 14, 67, 75–77] fall short; see Fig. 2 for typical predictions. This difficulty arises because cast and attached shadows are governed by different formation mechanisms: cast shadows are often driven by object boundaries and produce relatively contiguous regions of contrast, amenable to appearance-based detection. Attached shadows, by contrast, arise from the interplay between surface orientation and illumination. They follow object geometry closely, often appearing fragmented with weak contrast, and resist detection without explicit reasoning about scene geometry and lighting.

We therefore introduce a framework that jointly detects cast and attached shadows by modeling their physical dependence on light direction and surface geometry. The key insight is simple: under direct illumination, surfaces facing away from the light receive no direct light and therefore form attached shadows. This relationship works in both directions. Given a light direction[1] and surface normals, we can estimate a partial attached-shadow map. Conversely, given

[1] We assume a single dominant directional light source.



(a)Input (b)MTMT [4] (c)SDCM [77] (d)SILT [67] (e)Ours Cast (f)Ours Att.

Fig. 2: Existing shadow detection methods primarily focus on cast shadow detection and do not differentiate between cast and attached shadow types (b, c, d). In contrast, our method accurately segments cast and attached shadows separately (e, f).

observed shadows and scene geometry, we can partially reason about the light direction. We exploit this reciprocal relationship through a closed-loop, dual-module architecture, in which a shadow detection module and a light estimation module mutually refine each other across iterative passes.

To support training and evaluation, we contribute a dataset of 1,458 images with manually annotated cast and attached shadow masks, drawn from three existing benchmarks [14, 49, 55]. Experiments confirm that our iterative, geometry- and light-aware formulation outperforms prior methods on both shadow types.

Our contributions are:

- A joint framework for detecting cast and attached shadows through shared learning with light estimation.
- An iterative refinement scheme in which lighting and shadow cues mutually reinforce each other.
- A curated dataset with separate annotations for cast and attached shadows, enabling standardized evaluation.
- Our method outperforms previous methods on both shadow types, with at least a 33% reduction in attached-shadow BER.

2 Related Work

Shadow detection and removal [6, 11–13, 16, 21–23, 28, 40] are fundamental tasks in computer vision, where accurate shadow estimation is crucial for tasks such as scene understanding [20, 24, 26, 27] and generation [60, 62–66]. Earlier shadow detection studies [30–34, 43] extensively explored the relationship between lighting and shadows. Panagopoulos *et al.* [35] were among the first to jointly model shadow detection and light estimation using coarse scene geometry. However, their approach relied on simplified geometry and idealized physical models, which limited its ability to handle the complexities and variations in real-world images.

Recent deep learning advancements have significantly improved shadow detection [2, 14, 15, 25, 52, 74, 75]. Ding *et al.* [8] introduced an attentive recurrent GAN that iteratively detects and removes shadows. Chen *et al.* [4] leveraged multiple cues from shadow regions, edges, and shadow counts, using a student-teacher model. Zhu *et al.* [76] noted that deep shadow detectors were overly

reliant on intensity cues and proposed a feature decomposition and reweighting approach to reduce intensity bias. SDCM [77] used a complementary mechanism to jointly detect shadow and non-shadow regions by transferring deactivated intermediate features between branches. Sun *et al*. [46] focused on preserving multiscale contrast information by mapping RAW images to sRGB representations of varying intensities. More recently, SwinShadow [59] leveraged a transformer-based architecture with a shifted window mechanism to better detect adjacent shadows by capturing hierarchical contextual details. In addition, several approaches have targeted more specialized tasks. [53–55] focused on the instance shadow detection task, concentrating on cast shadows associated with annotated objects. Wang *et al*. [56] proposed MetaShadow, which studies object-centered shadow reasoning by jointly addressing shadow detection, removal, and synthesis within a unified framework.

While these recent methods have significantly advanced shadow detection, they do not explicitly address the unique challenge of detecting attached shadows. Several methods and datasets acknowledge the importance of attached shadows. Yang *et al*. [67] annotated attached shadows for the SBU-test set and proposed a method that uses predicted shadows as updated training labels. Hu *et al*. [14] introduced a benchmark in which a large portion of the shadows are attached shadows. However, these approaches still treat cast and attached shadows uniformly, ignoring their distinctions.

Estimated lighting has been widely used in computer vision tasks. Existing illumination representations can be broadly categorized into three types: environment maps [44, 50], light probes [1, 38], and parameterized lighting models [7, 9, 71]. In this paper, we adopt a three-dimensional light-direction parameterization to model a dominant distant directional light, typical of outdoor daylight, and to provide a controlled, interpretable link between illumination and scene geometry. Importantly, shadow understanding under this single-direction assumption remains actively studied [61], and attached shadow detection is still challenging even in this setting.

3 Method

3.1 Framework Overview

Our framework detects both cast and attached shadows by jointly learning shadow detection and light estimation from a single RGB image and its corresponding normal map (Fig. 3). We define attached shadows as shadows on the object itself (typically on surface regions oriented away from the light), and cast shadows as shadows projected onto external surfaces. Attached shadows depend on surface orientation and lighting, motivating our geometry- and light-aware design. We assume a single scene-wide directional light shared across the image, and define $\boldsymbol{\ell}$ to point from the light toward the scene.

Our shadow detection module is formulated as a multi-class segmentation task over $\{\text{bg}, \text{cast}, \text{attached}\}$, taking the RGB image and normal map as input.

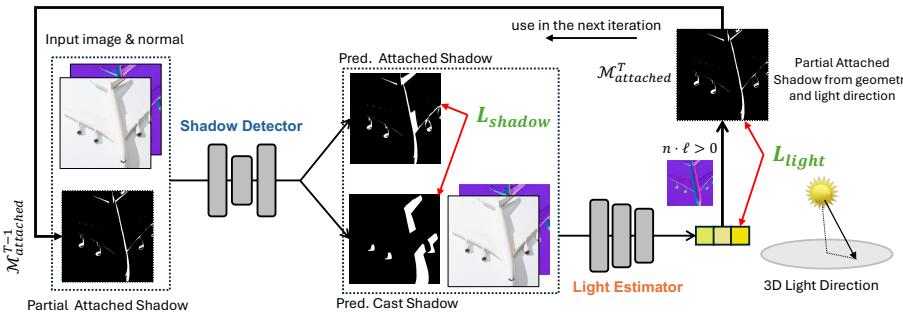


Fig. 3: Framework overview. Our network consists of a shadow detection module and a light estimation module. The detector predicts cast and attached shadows, while the light module estimates a 3D light direction and generates a geometry-based partial attached shadow map. This partial map is fed back to the detector as an additional input during iterative training, enabling progressive refinement.

Our light estimation module leverages the normal map and predicted shadows to estimate the light direction as a three-dimensional vector. Using the estimated light direction and surface normals, we generate a geometry-derived *partial attached shadow map* from a simple normal-light alignment cue. This partial map is incorporated as an additional input to refine shadow detection, while the predicted shadows provide auxiliary cues for light estimation. The two modules operate in a closed loop and are iteratively refined over multiple forward passes, improving both shadow detection and light estimation.

3.2 Iterative Training

Shadow and illumination serve as mutual cues for estimating each other [35]. Similarly, our framework jointly and iteratively refines shadow detection and light estimation.

Each training step consists of multiple iterations. In each iteration, we use the predicted light direction and surface normals to generate a *partial attached shadow map* derived from geometry and light direction. This map highlights pixels that are likely to belong to attached shadows based purely on local surface orientation and the light direction. It is not a complete attached shadow mask because it does not model visibility or geometric blocking; thus, it cannot capture cases where one surface region blocks light from reaching another. Still, it provides reliable local cues near contact regions and boundaries, and is fed to the shadow detection module in the next iteration as an additional input to predict the complete cast and attached shadow masks. Because this map is generated from the current light estimate during training, the detector learns to use imperfect geometry cues.

Specifically, given a light direction vector $\boldsymbol{\ell} \in \mathbb{R}^3$ pointing from the light source toward the surface and surface normals $\boldsymbol{n} \in \mathbb{R}^{H \times W \times 3}$, the partial attached

shadow map, denoted as $\mathcal{M}_{\text{attached}}$, includes surface points oriented away from the light source as:

$$\mathcal{M}_{\text{attached}} = \begin{cases} 1, & \boldsymbol{n} \cdot \boldsymbol{\ell} > 0 \\ 0, & \boldsymbol{n} \cdot \boldsymbol{\ell} \leq 0 \end{cases} \tag{1}$$

This geometry-based map serves as a coarse attached-shadow prior. As the estimated light direction becomes more accurate across iterations, the map is progressively refined, leading to improved shadow detection and, in turn, better light estimation. In the first iteration, the partial attached-shadow map is set to an all-ones map.

3.3 Training Objectives

We jointly optimize the two modules with complementary objectives for shadow detection and light estimation. The shadow loss enforces accurate and well-separated segmentation of cast and attached shadows, while the light loss supervises the estimated light direction and regularizes it for physical plausibility. Together, these objectives encourage stable convergence of the iterative refinement process described above.

Shadow Detection Loss. We supervise the shadow detector at two complementary levels. First, for global shadow segmentation (shadow vs. background), we aggregate subclass logits with the log-sum-exp (LSE): $\text{LSE}(a, b) = \log(e^a + e^b)$. Let $z_{\text{bg}}, z_{\text{cast}}, z_{\text{att}} \in \mathbb{R}$ be per-pixel logits; we define:

$$s = \text{LSE}(z_{\text{cast}},\, z_{\text{att}}) - z_{\text{bg}}. \tag{2}$$

We match s to the union ground-truth shadow mask $y_{\text{union}} \in \{0, 1\}$ using a binary cross-entropy (BCE) term plus a Dice [45] regularizer:

$$\mathcal{L}_{\text{seg}} = \text{BCE}(s,\, y_{\text{union}}) + \lambda_{\text{Dice}}\, \text{Dice}(s,\, y_{\text{union}}). \tag{3}$$

Second, to distinguish shadow types (cast vs. attached), we apply a standard multi-class cross-entropy (CE) on the full logits with per-pixel labels $y_{\text{type}} \in \{\text{bg}, \text{cast}, \text{att}\}$. In addition, we impose a class-conditional margin on the cast vs. attached logits to sharpen their separation. Let $d^{(i)} = z^{(i)}_{\text{cast}} - z^{(i)}_{\text{att}}$, and let Ω_{cast} and Ω_{att} be the index sets of pixels labeled cast and attached, respectively. With margin $m = 0.2$, we have:

$$\mathcal{L}_{\text{dist}} = \frac{1}{|\Omega_{\text{cast}}|} \sum_{i \in \Omega_{\text{cast}}} \max\bigl(0,\, m - d^{(i)}\bigr) + \frac{1}{|\Omega_{\text{att}}|} \sum_{i \in \Omega_{\text{att}}} \max\bigl(0,\, m + d^{(i)}\bigr), \tag{4}$$

$$\mathcal{L}_{\text{type}} = \text{CE}(\mathbf{z},\, y_{\text{type}}) + \lambda_{\text{dist}}\, \mathcal{L}_{\text{dist}}. \tag{5}$$

Together, this supervision encourages robust recovery of overall shadow extent while explicitly teaching the model to separate attached from cast shadows. The total shadow loss is therefore:

$$\mathcal{L}_{\text{shadow}} = \mathcal{L}_{\text{seg}} + \mathcal{L}_{\text{type}}. \tag{6}$$

Light Estimation Loss. We constrain the light estimator with three complementary losses. First, we encourage light cues to localize attached shadows by aligning $\mathcal{M}_{\text{attached}}$ with the ground-truth attached shadow mask $y_{\text{att}} \in \{0, 1\}$ via a weighted BCE. Second, we regress the predicted light direction $\hat{\boldsymbol{\ell}}$ to a heuristic target $\boldsymbol{\ell}^\star$ (from geometry; see Sec. 4 for details) with an ℓ_1 loss. Third, we enforce a unit norm:

$$\mathcal{L}_{\text{att}} = \text{BCE}_w(\mathcal{M}_{\text{attached}}, y_{\text{att}}), \quad \mathcal{L}_{\text{dir}} = \left\|\hat{\boldsymbol{\ell}} - \boldsymbol{\ell}^\star\right\|_1, \quad \mathcal{L}_{\text{unit}} = (\|\hat{\boldsymbol{\ell}}\|_2 - 1)^2. \quad (7)$$

The overall light loss is then:

$$\mathcal{L}_{\text{light}} = \lambda_{\text{att}}\mathcal{L}_{\text{att}} + \lambda_{\text{dir}}\mathcal{L}_{\text{dir}} + \lambda_{\text{unit}}\mathcal{L}_{\text{unit}}. \quad (8)$$

Finally, the full training objective is:

$$\mathcal{L}_{\text{total}} = \mathcal{L}_{\text{shadow}} + \mathcal{L}_{\text{light}}. \quad (9)$$

4 Dataset

We introduce the first dataset specifically curated for cast and attached shadow detection, consisting of 1,166 training and 292 test images. Each image is paired with (i) a surface normal map, (ii) a ray-based heuristic 3D light direction, (iii) binary cast and attached shadow masks, and (iv) an "undefined" shadow mask. Fig. 4 shows example annotations.

Our dataset is compiled from three public sources: 220 images from WSRD [49] (paired shadow/shadow-free images), 710 images from SOBA [55] (shadow images with instance-level cast masks), and 528 images from CUHK [14] (scene-level full-shadow masks).

Accurately annotating cast and attached shadows per pixel in natural scenes is highly labor-intensive due to mixed shadow types. To simplify annotation, we restrict fine-grained labeling to foreground objects: we manually mark the cast shadows and attached shadows associated with the annotated objects. All remaining shadow pixels not attributable to these objects are labeled as *undefined shadows*. We use undefined shadows only for full-shadow supervision and evaluation, and exclude them from cast/attached training and evaluation. This avoids ambiguous ownership and provides a fairer assessment of cast/attached separation. Additional details on data preparation are provided in the supplementary material.

Normal Maps. Since geometry is crucial for identifying attached shadows, we use a recent foundation model [69] to predict relative depth, which we convert to normal maps.

Object Masks. We extract object masks using BiRefNet [73]. These masks are used only for annotation and evaluation.

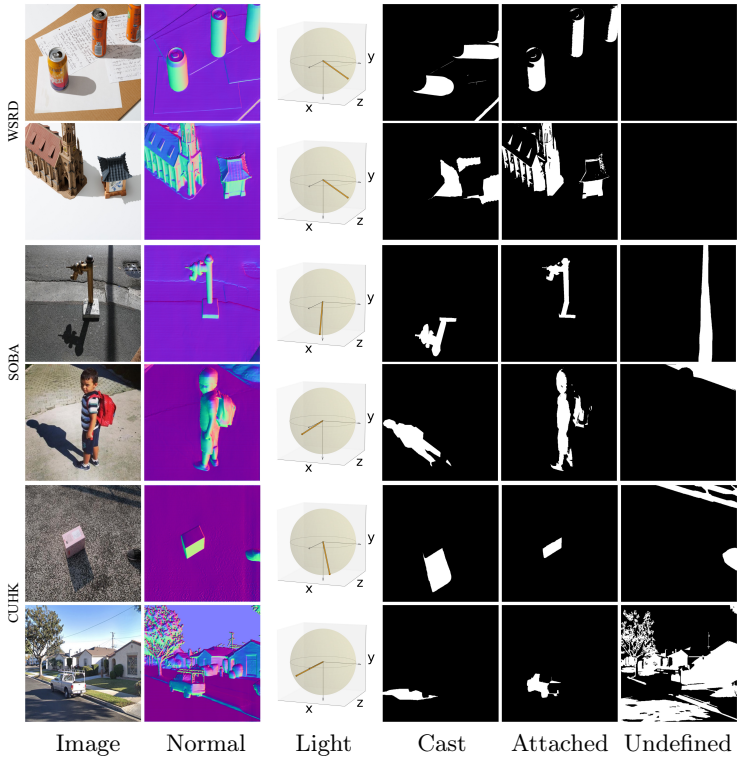


Fig. 4: Examples of our proposed dataset. We curate the dataset from WSRD [49], SOBA [55], and CUHK [14]. Each image is paired with its normal map, light direction, and cast/attached/"undefined" shadow masks. Light direction is camera-centric: $+x$ right, $+y$ down, $+z$ inward.

Cast and Attached Shadow Masks. Using the object masks, we manually annotate and refine cast and attached shadow masks for SOBA and CUHK. For WSRD, which lacks shadow masks, we derive full-shadow masks by color-space subtraction between shadow and shadow-free images, and then annotate cast and attached components.

Light Directions. WSRD images are captured under a calibrated fixed-lighting system [49]; therefore, we manually compute ground-truth 3D light directions. For SOBA and CUHK, we estimate a heuristic 3D direction in two steps. **(i) In-plane direction.** We compute a 2D image-plane direction by connecting the centroid of a foreground object to the centroid of its cast shadow. Under a directional-light assumption, a cast shadow can be viewed as the object translated along the illumination direction and projected onto the receiving surface; thus, the object-to-shadow displacement provides the illumination ray's image-plane projection. **(ii) Depth sign.** We infer the third component from the relative depth between the object region and its cast shadow region. If the shadow lies

Table 2: Quantitative comparison with state-of-the-art methods on our dataset. We report BER↓ and F1↑ for full, cast, and attached shadows. Methods fine-tuned on our training set are marked with †. Best results are in **bold**.

	Full		Cast		Attached	
Methods	**BER↓**	**F1↑**	**BER↓**	**F1↑**	**BER↓**	**F1↑**
BDRAR [75]	21.29	70.53	7.23	79.64	35.41	52.32
DSD [74]	22.53	68.75	7.83	80.10	35.93	51.74
FSDNet [14]	24.46	66.09	10.51	79.16	37.53	46.24
MTMT [4]	33.10	50.00	15.16	74.66	42.02	38.10
FDRNet [76]	23.69	65.69	8.95	71.65	34.82	55.15
SDCM [77]	24.27	66.51	7.88	83.42	36.83	49.02
SILT [67]	20.20	71.51	4.64	80.39	32.70	60.23
BDRAR†	8.15	83.95	5.18	72.86	20.75	82.69
FSDNet†	10.17	85.10	5.82	81.94	19.49	80.57
FDRNet†	8.62	83.00	4.65	73.27	23.11	81.42
SILT†	6.51	82.98	**4.52**	68.31	26.57	80.72
Ours	**6.50**	**86.61**	5.04	**85.46**	**12.92**	**86.49**

on a surface deeper than the object, the illumination has a component pointing into the scene; if it lies shallower, the component points toward the camera. Combining this signed component with the in-plane vector and normalizing yields a 3D unit direction in our camera-centric frame ($+x$ right, $+y$ down, $+z$ inward).

5 Experiments and Results

Implementation Details. The proposed framework is implemented using PyTorch [36]. The shadow detection backbone follows SILT [67], and the light estimation module uses ConvNeXt-S [29]. We train with Adam [18] (learning rate 5×10^{-4}, 20 epochs, batch size 4). We set λ_{Dice}, λ_{dist}, λ_{att}, λ_{dir}, and λ_{unit} to 0.1, 0.2, 0.4, 0.5, and 0.1, respectively. Additional details are provided in the supplementary.

Evaluation Methods and Metrics. We compare against seven state-of-the-art methods: BDRAR [75], DSD [74], FSDNet [14], MTMT [4], FDRNet [76], SDCM [77], and SILT [67]. We evaluate all baselines with their SBU-pretrained weights and additionally fine-tune BDRAR, FSDNet, FDRNet, and SILT on our training set with full-shadow supervision (marked with † in Tab. 2).

We report the F1 score, $F1 = \frac{2TP}{2TP+FP+FN}$, and the balanced error rate (BER), $\text{BER} = 100 \times \big(1 - \frac{1}{2}\big[\frac{TP}{TP+FN} + \frac{TN}{TN+FP}\big]\big)$, where TP, TN, FP, and FN denote true positives, true negatives, false positives, and false negatives.

For prior baselines that output a single shadow mask, we split their predictions using the object mask. Cast evaluation excludes the undefined region, and attached evaluation is restricted to the object region.

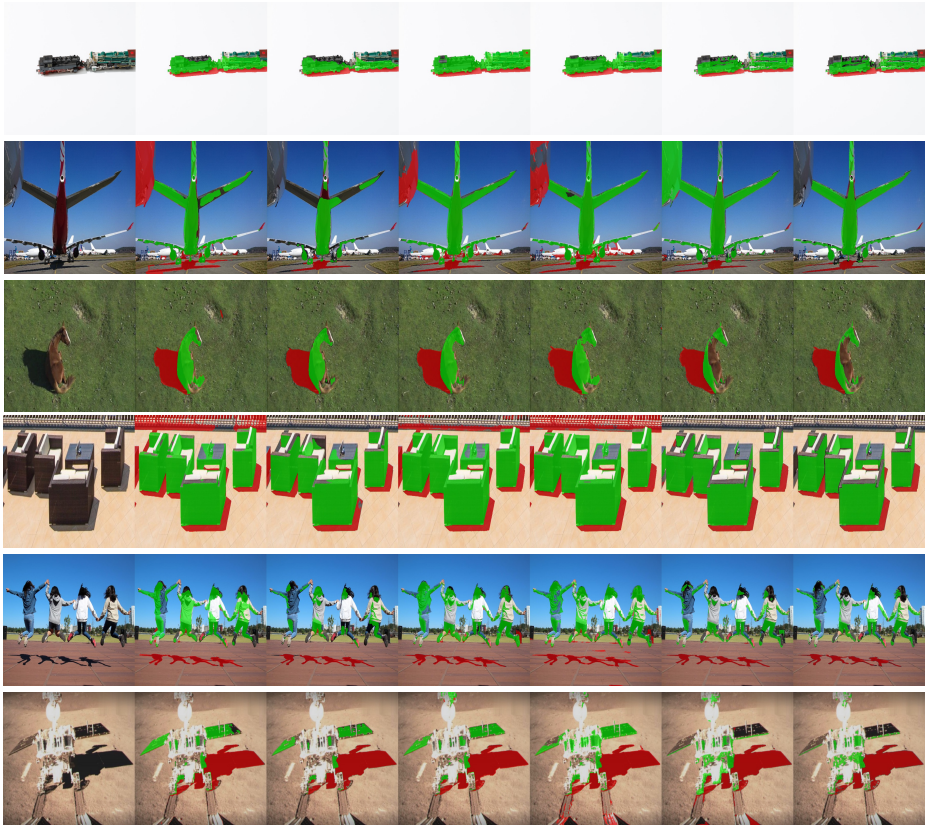


Fig. 5: Qualitative comparison of our method with retrained BDRAR [75], FSDNet [14], FDRNet [76], and SILT [67] on our dataset. Predicted masks are overlaid on the input image (*green: attached, red: cast*). Our geometry- and light-aware iterative framework produces more accurate attached-shadow boundaries.

5.1 Comparison with SOTA methods

Quantitative Comparisons. Tab. 2 reports BER and F1 scores for full, cast, and attached shadows. Our method achieves the best performance on full and attached shadows in both metrics and the strongest cast F1, while its cast BER remains comparable to prior approaches.

We first evaluate the SBU-pretrained baselines, which are cast-focused. All methods show a clear gap between cast and attached performance, with attached-shadow BER worse by about 20–30 points. These models primarily capture cast shadows, which often appear as contiguous, lower-intensity regions, and only detect attached shadows when they visually resemble cast shadows. This highlights the limitations of cast-biased training data for attached-shadow detection. We then retrain the baselines on our data using full-shadow supervision. This

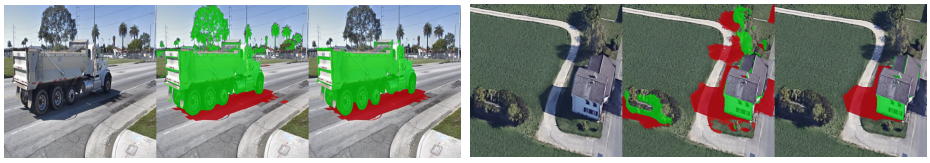


Fig. 6: Examples with foreground-only annotations. Although supervision is limited to the foreground objects, our method produces coherent cast and attached shadow predictions over the full image.

narrows the gap, but the baselines still struggle with attached shadows. A key limitation is that they treat the two shadow types uniformly and ignore that attached shadows are governed by surface orientation and contact rather than occlusion.

In contrast, our method leverages geometry and lighting by using surface normals and estimating a light direction. These physical cues let the model reason about where attached shadows should occur while preserving cast performance. As a result, attached shadow BER is reduced by at least 33% relative to retrained baselines, while maintaining strong performance on full and cast shadows.

Qualitative Comparisons. Fig. 5 shows visual comparisons between four retrained baselines and our method. The baselines produce a single shadow mask, so we use the object mask to split their outputs into cast and attached regions. Our method follows occluder geometry and the estimated light direction, producing geometry-consistent attached-shadow boundaries on surfaces facing away from the light (rows 1–2). In contrast, the baselines rely mainly on image appearance and tend to mark dark regions as shadows, even when those surfaces are lit (rows 3–5). By using surface normals, an estimated light direction, and separate predictions for cast and attached shadows, our method improves attached shadow quality while maintaining strong cast predictions.

We further show qualitative results in Fig. 6 where the ground-truth annotations cover only foreground objects, yet our method correctly assigns cast and attached labels across the remaining undefined shadow regions. This suggests a potential path toward reducing dense annotation effort through pseudo-labels or weak supervision.

5.2 Ablation Studies

To validate the effectiveness of our framework design, we conduct ablation studies to analyze the contributions of (i) surface-normal guidance, (ii) the iterative learning scheme, and (iii) each loss component.

Effect of geometry guidance. We examine the role of surface normals as geometry guidance. Removing surface normals reduces our model to a standard multi-class segmentation network trained with class-specific labels. This substantially

Table 3: Ablation of our geometry- and light-aware framework. We evaluate the impact of (i) removing surface normals, (ii) varying the number of refinement iterations, and (iii) disabling individual loss terms. We report BER↓ and F1↑ for full, cast, and attached shadow detection.

	Full		Cast		Attached	
Setting	**BER↓**	**F1↑**	**BER↓**	**F1↑**	**BER↓**	**F1↑**
Geometry						
No Normal	7.60	85.46	7.82	79.33	20.87	77.07
Iterations						
Non-iterative	7.57	85.99	6.14	87.75	15.10	83.91
2 iterations	6.63	87.77	5.41	86.75	13.22	85.63
3 iterations (final)	6.50	86.61	5.04	85.46	12.92	86.49
5 iterations	6.11	87.14	5.83	85.57	13.51	85.74
Loss terms						
No $\mathcal{L}_{\text{dist}}$	7.19	86.25	6.16	85.69	13.45	85.38
No $\mathcal{L}_{\text{att}}$	6.89	87.03	5.81	85.26	14.61	84.24
No $\mathcal{L}_{\text{dir}}$	7.50	86.42	4.97	85.02	15.26	83.59

degrades performance across metrics, with the largest drop on attached shadows, yielding results comparable to retrained baselines. This confirms that surface normals provide strong spatial priors for separating cast and attached shadows.

Effect of iterative learning. We evaluate a non-iterative variant that jointly trains shadow detection and light estimation with normal maps, but does not feed the predicted partial attached map back into the detector. As shown in Tab. 3, this setting outperforms the variant without normal guidance, confirming the benefit of geometry awareness. We then vary the number of refinement iterations (2, 3, and 5). Iterative feedback improves predictions: two iterations provide the largest gain, and performance saturates at three iterations, as also shown by the intermediate results in Fig. 7. Increasing to five iterations slightly improves full-shadow accuracy but reduces class-specific performance, suggesting over-refinement of the partial map. In terms of efficiency, runtime increases approximately linearly with the number of iterations; our 3-step setting is 3× slower than the non-iterative model (0.55 s vs. 0.18 s per image). Overall, geometry provides the key prior, and iterative refinement further improves segmentation.

Effect of loss design. We ablate each loss term individually during training. Removing any single term reduces performance, indicating that the losses are complementary. $\mathcal{L}_{\text{dist}}$ encourages separation between cast and attached logits via a class-conditional margin, leading to a clearer decision boundary. The light-related losses, $\mathcal{L}_{\text{att}}$ and $\mathcal{L}_{\text{dir}}$, guide the light estimator to produce spatially coherent partial maps by aligning outputs with ground-truth cues and enforcing directional consistency. Together, these objectives promote effective geometry–light interaction and more reliable shadow predictions.

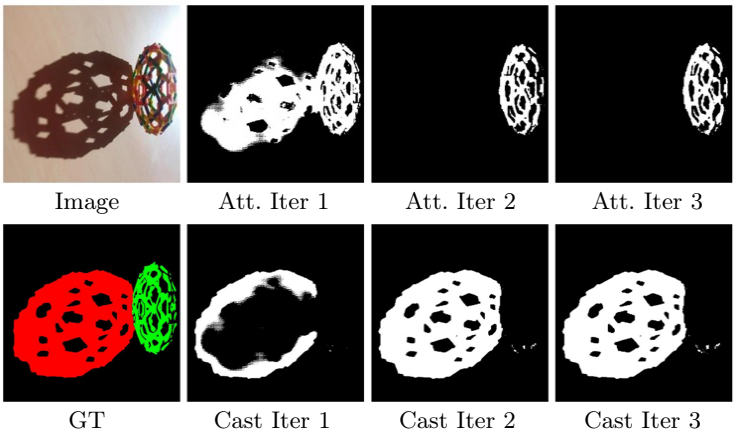


Fig. 7: Effectiveness of the iterative learning scheme. Our proposed feedback mechanism progressively refines the shadow predictions, showing clear visual improvements at the second iteration and stabilization at the third.

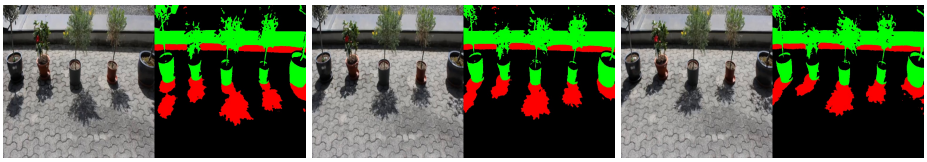


Fig. 8: Cross-dataset generalization on SBU-TimeLapse [23]. We apply our model to a static-camera video with time-varying shadows and visualize predictions at different time steps. The results remain temporally consistent and show coherent cast and attached shadow separation across the sequence.

5.3 Cross-dataset Generalization

To assess generalization beyond our training data, we conduct experiments on SBU-TimeLapse [23], a static-scene video dataset with time-varying shadows. We run our model on each frame independently. As shown in Fig. 8, our predictions remain temporally consistent while producing accurate cast and attached shadow separation across the sequence, indicating robustness to temporal shadow variation. Additional qualitative results are provided in the supplementary.

5.4 Shadow Removal Application

Shadow masks are widely used in downstream tasks. To demonstrate the practical value of separating attached shadows, we study shadow removal as an example. We guide an off-the-shelf shadow removal model [10] using a *joint* shadow mask, and then refine the result within the object region using the *attached* shadow mask. Because our data do not provide shadow-free ground truth for



Fig. 9: User study example. Each question shows the input image and object mask, along with two candidate results: one guided by a joint shadow mask and the other guided by separate cast/attached masks with object-region refinement. Candidate order is randomized, and participants select the more natural output.

Table 4: User study on shadow removal. Participants were asked to choose the more natural result between the joint-mask guidance (Joint) and separate-mask guidance with attached-region refinement (Separate).

Method	Preference (%)
Joint	19.3
Separate	80.7

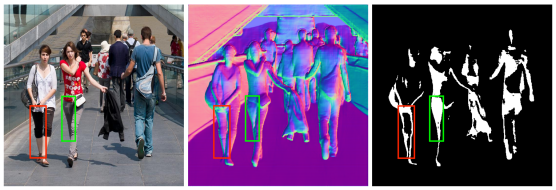


Fig. 10: Limitations. Attached-shadow errors can arise from inaccurate surface normals, such as flipped normal directions that lead to incorrect attached-shadow predictions.

quantitative evaluation, we conduct a user study in which participants choose the more natural of the two outputs (see Fig. 9). As shown in Tab. 4, participants prefer the result that uses the attached mask for refinement in 80.7% of comparisons. This outcome underscores the importance of separating cast and attached shadows: it enables targeted refinement on the object while removing cast shadows, leading to more realistic results.

6 Limitations

As an initial step toward detecting both cast and attached shadows, our framework has certain limitations. First, it relies on scene geometry derived from normal maps generated by an off-the-shelf model [69]. However, this foundation model does not always yield accurate surface orientations, and such errors can propagate to our predictions, as illustrated in Fig. 10. Improving the reliability of geometric cues through better normal estimation or geometry refinement is a promising direction for future work. Second, our approach assumes a single directional light source, which may not generalize well to complex illumination settings, including multi-source indoor lighting, soft shadows from extended light sources, and low-light/night-time scenes with strong indirect illumination. Future work could extend the lighting formulation beyond a single directional

source by modeling multiple or area lights, and broaden training data to cover more diverse illumination conditions.

7 Conclusion

We introduced a geometry- and light-aware framework for separately detecting cast and attached shadows, addressing the gap where most prior shadow detectors predict a unified mask or remain cast-focused. Motivated by the relationship between illumination, surface geometry, and shadows, our method jointly learns shadow segmentation and light estimation: the estimated light direction and surface normals yield a geometry-derived partial attached shadow map, which is fed back to refine detection, while predicted shadows provide cues for updating the light direction. This closed-loop, iterative formulation, together with explicit supervision for cast/attached separation, consistently improves attached-shadow detection while maintaining strong cast-shadow performance, as shown by comparisons to state-of-the-art baselines. To support future research and model development, we introduce a new dataset with high-quality separate annotations for cast and attached shadows.

Acknowledgements

This work was supported in part by the CCI startup fund at UNC Charlotte and NSF Grant IIS-2212046.

Cast and Attached Shadow Detection via Iterative Light and Geometry Reasoning

Supplementary Material

Shilin Hu[1], Jingyi Xu[1], Sagnik Das[1], Dimitris Samaras[1†], and Hieu Le[2†]

[1] Stony Brook University, Stony Brook NY 11794, USA
[2] UNC Charlotte, Charlotte NC 28223, USA
{shilhu,jingyixu,sadas,samaras}@cs.stonybrook.edu, hle40@charlotte.edu

In this supplementary material, we provide the following:

1. Additional visual results, including results for the **shadow removal application**, **cross-dataset** evaluation, and **qualitative** comparisons.
2. Additional details on the framework design and evaluation, including the detailed **model architecture**, full **quantitative comparisons**, **computational overhead**, and **light estimation** performance.
3. Details of **dataset acquisition and curation**.
4. In addition to this PDF, we provide animated GIF examples illustrating cast and attached video shadow detection. Since these videos do not include attached shadow annotations, quantitative evaluation is not reported.

1 More Qualitative Results

Shadow Removal. We conduct a user study to evaluate shadow removal performance. The study contains a pool of 40 questions. Each participant evaluates 20 randomly selected questions from this pool, and the presentation order of the unified and separate removal results is randomized. In total, we collected 259 votes, of which 209 favor the separate refinement over the unified refinement, corresponding to 80.7%.

† Equal advising.



Fig. 1: Shadow removal application. Using a separate attached shadow mask for targeted refinement within the object region can produce more natural shadow removal.

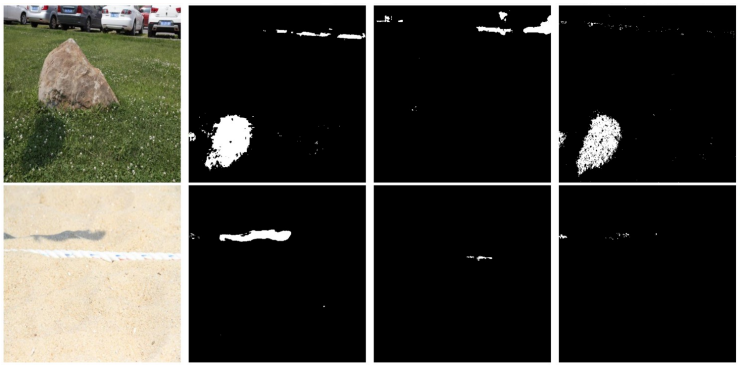


Fig. 2: Qualitative cross-dataset results on SRD [40], an image shadow detection dataset.

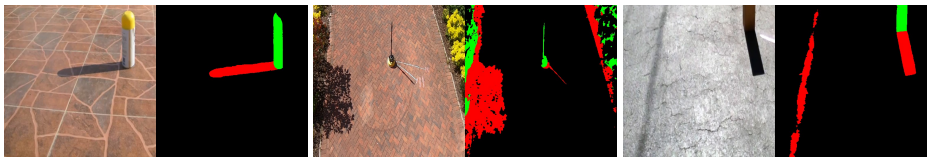


Fig. 3: Qualitative cross-dataset results on SBU-TimeLapse [23], a video shadow detection dataset with static scenes.



Fig. 4: Qualitative cross-dataset results on ViSha [3], a video shadow detection dataset with dynamic scenes.

Additional results for shadow removal using ShadowFormer [10] with a unified shadow mask and separate cast and attached shadow masks are shown in Fig. 1. These examples demonstrate that using a separate attached shadow mask for refinement within the object region leads to more natural color recovery.

Cross-dataset. Additional cross-dataset results are shown in Fig. 2, Fig. 3, and Fig. 4. We evaluate our method on the image shadow detection dataset SRD [40], as well as the video shadow detection datasets SBU-TimeLapse [23] and ViSha [3]. The results qualitatively show that our method generalizes across both image and video settings. Additional video results on SBU-TimeLapse [23] and ViSha [3] are provided in the `gif` folder for better visualization.

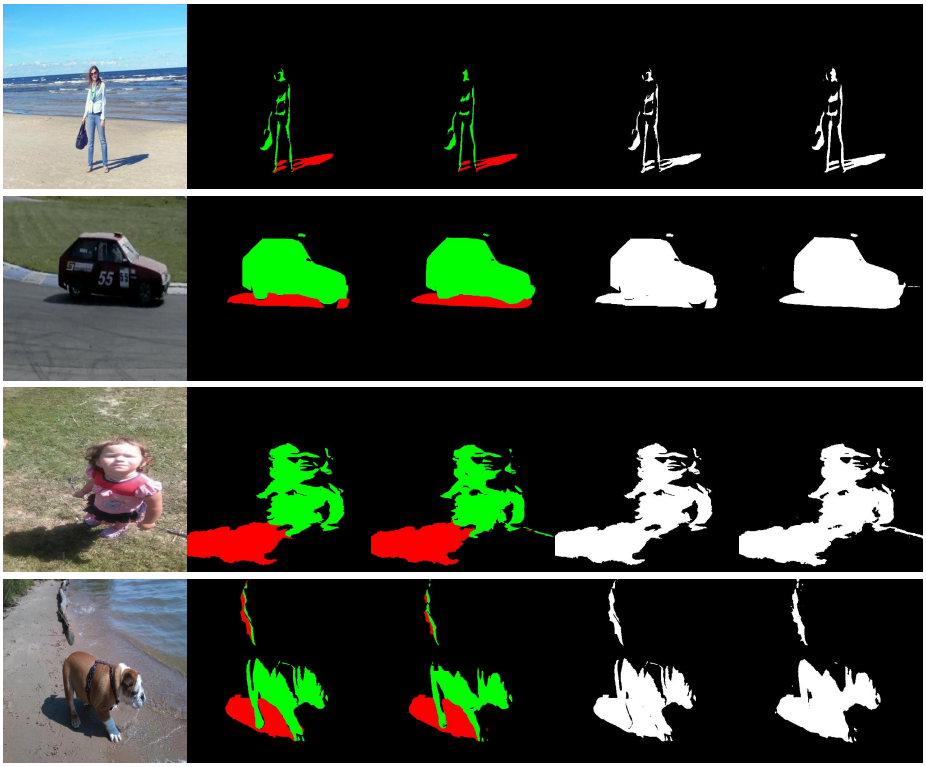


Fig. 5: Additional qualitative examples of cast, attached, and full shadow predictions across diverse scenes in our dataset.

Qualitative. Additional qualitative results for cast, attached, and full shadow detection are shown in Fig. 5, Fig. 6, and Fig. 7. Each figure displays the input image, ground-truth cast and attached shadow masks, our predicted cast and attached masks, and the corresponding ground-truth and predicted full shadow masks across diverse scenes.

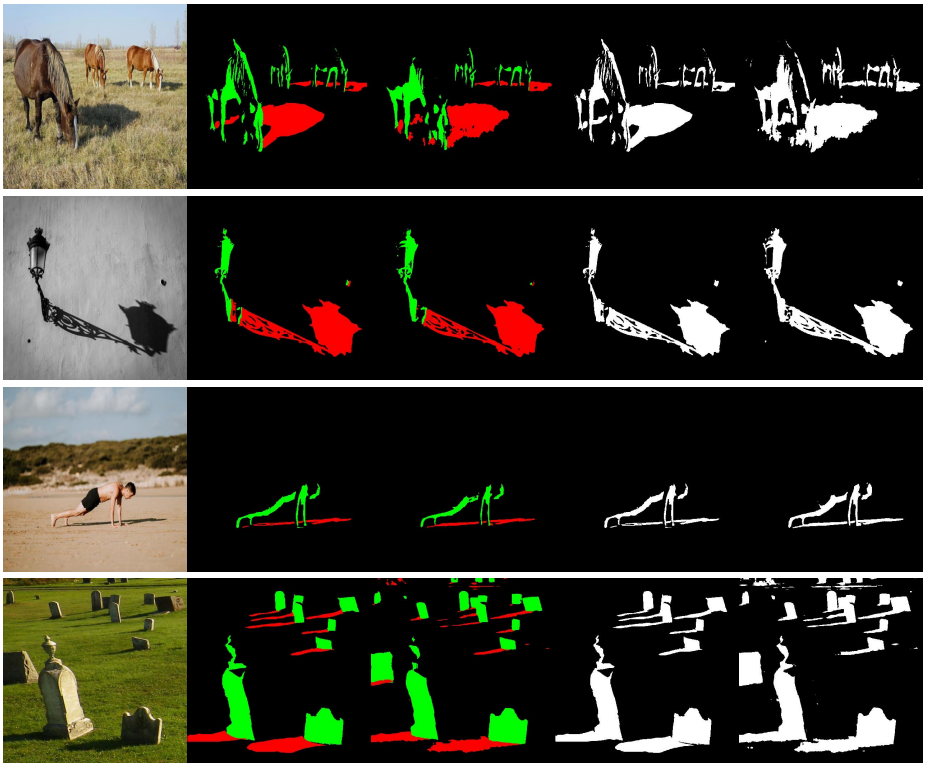


Fig. 6: Additional qualitative examples of cast, attached, and full shadow predictions across diverse scenes in our dataset.

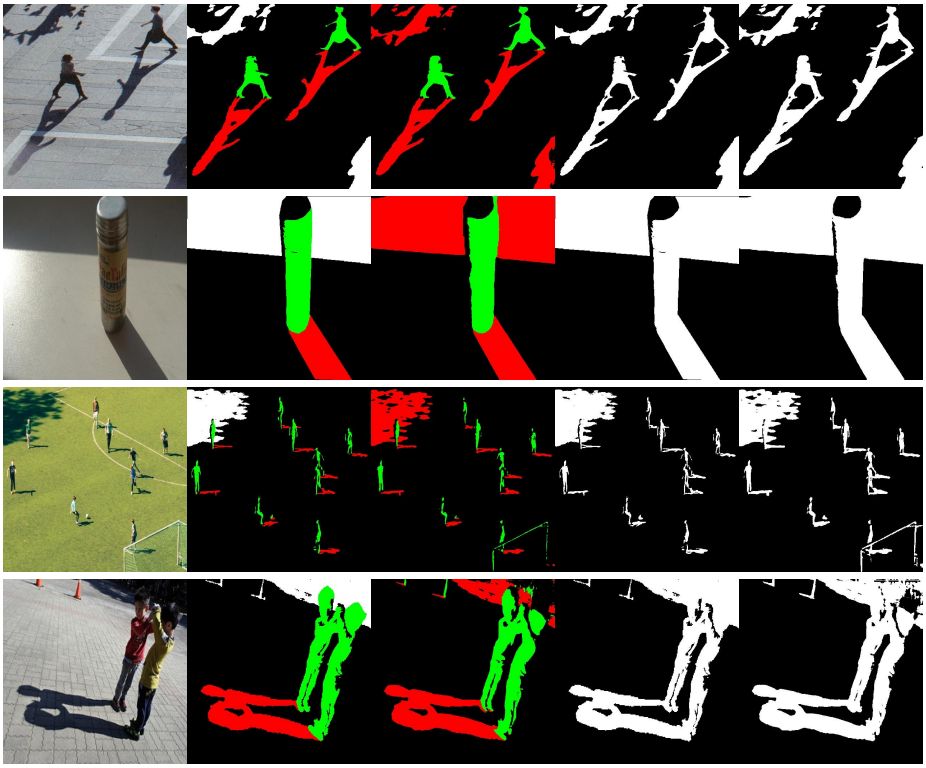


Fig. 7: Additional qualitative examples of cast, attached, and full shadow predictions across diverse scenes in our dataset. Undefined shadows are marked as white in GT.

2 Framework Design and Evaluation

We introduce a joint framework for shadow detection and light estimation, where the shadow detection module simultaneously predicts both cast and attached shadows. All experiments are conducted on NVIDIA TITAN RTX GPUs. While baseline models run on a single GPU, our method requires two GPUs for training. In this section, we detail the modifications to the network modules and provide additional evaluations on different shadow-detection configurations, light-estimation performance, and the computational overhead.

2.1 Network Architecture

The shadow detection module is adapted from the SILT model [67], which features an encoder-decoder architecture with skip connections. The encoder is based on PVT-b5 [57], and we modify its first layer to incorporate additional input from the normal map and iterative feedback from the prior mask. The remaining encoder layers retain the original architecture, are initialized from SBU pre-trained weights, and are fine-tuned with a learning rate that is 0.05 times that used for the rest of the framework. Only minimal changes are made to the decoder: we introduce a multi-channel segmentation head in the final layer with separate outputs for background, cast shadows, and attached shadows.

The light estimation module is adapted from ConvNeXt-S [29], with modifications to the input layer and the final output layer. The output of the light estimation module is a three-dimensional vector, where each dimension represents one component of the light direction.

For retraining prior methods [14,67,75,76], we use the full shadow mask (cast shadow + attached shadow + undefined shadow) as the supervision signal, as these methods formulate shadow detection as binary segmentation.

2.2 More Shadow Detection Evaluation

Tab. 1 reports the full set of metrics for our comparisons with previous methods, retrained baselines, and different configurations of our proposed framework. We report the *Precision*, *Recall*, *F1 score*, *BER*, and error rate for shadow and non-shadow regions for full-shadow, cast-shadow, and attached-shadow detection.

2.3 Computational Overhead

Tab. 2 summarizes the computational overhead across different configurations. In the non-iterative setting, our method introduces only a marginal increase of roughly 0.04 seconds per image over the retrained SILT baseline, mainly because of the lightweight jointly learned light-estimation module. In the iterative setting, inference time scales predictably with the number of refinement steps. Our final configuration with three iterations achieves the best overall tradeoff between performance and efficiency, with an inference time of 0.545 seconds per image.

Table 1: Quantitative results for shadow detection methods. We report the balanced error rate (BER), Precision (P), Recall (R), and F-measure (F) for full, cast and attached shadow detection. † denotes retraining on our data using the full-shadow mask.

Methods	Full						Cast						Attached					
	BER	**S**	**NS**	**P**	**R**	**F1**	**BER**	**S**	**NS**	**P**	**R**	**F1**	**BER**	**S**	**NS**	**P**	**R**	**F1**
BDRAR [75]	21.29	39.68	2.90	84.91	60.32	70.53	7.23	12.35	2.12	72.97	87.65	79.64	35.41	61.83	8.99	83.17	38.17	52.32
FSDNet [14]	24.46	46.83	2.09	87.30	53.17	66.09	10.51	19.53	1.49	77.89	80.47	79.16	37.53	68.14	6.92	84.27	31.86	46.23
MTMT [4]	33.10	64.15	2.05	82.59	35.85	50.00	15.16	29.07	1.25	78.81	70.93	74.66	42.02	74.55	9.50	75.71	25.45	38.10
FDRNet [76]	23.69	42.77	4.60	77.10	57.23	65.69	8.95	14.41	3.49	61.61	85.59	71.65	34.82	58.18	11.45	80.95	41.82	55.15
SDCM [77]	24.27	46.58	1.95	88.10	53.43	66.51	7.88	14.48	1.28	81.42	85.52	83.42	36.83	65.16	8.50	82.66	34.84	49.02
SILT [67]	20.20	36.67	3.73	82.12	63.32	71.51	4.64	6.75	2.54	70.64	93.25	80.39	32.70	51.92	13.47	80.59	48.08	60.23
BDRAR†	8.15	9.51	6.79	78.30	90.49	83.95	5.18	6.20	4.16	59.57	93.80	72.86	20.75	11.10	30.40	77.28	88.91	82.69
FSDNet†	10.17	17.11	3.22	87.43	82.89	85.10	5.82	9.66	1.97	74.96	90.34	81.94	19.49	23.64	15.34	85.27	76.36	80.57
FDRNet†	8.62	9.96	7.28	76.98	90.04	83.00	4.65	5.10	4.20	59.67	94.90	73.27	23.11	9.90	36.32	74.27	90.10	81.42
SILT†	6.51	3.11	9.91	72.56	96.89	82.98	4.52	3.39	5.64	52.84	96.61	68.31	26.57	3.36	49.78	69.31	96.64	80.72
BDRAR†+Normal	7.44	7.89	6.99	78.09	92.11	84.52	4.63	4.96	4.29	59.14	95.04	72.91	19.70	8.19	31.21	77.38	91.81	83.98
SILT†+Normal	8.53	7.57	9.48	72.51	92.43	81.26	6.54	7.05	6.02	50.23	92.95	65.20	22.79	6.68	38.90	73.62	93.32	82.31
Ours No Normal	7.60	10.14	5.07	81.46	89.86	85.46	7.82	13.74	1.90	73.44	86.26	79.33	20.87	29.25	12.49	84.62	70.75	77.07
Ours Non-iterative	7.57	10.52	4.61	82.78	89.48	85.99	6.14	11.47	0.81	86.98	88.53	87.75	15.10	20.50	9.70	88.84	79.50	83.91
Ours No $\mathcal{L}_{\text{dist}}$	7.19	9.63	4.76	82.48	90.37	86.25	6.16	11.20	1.12	82.79	88.80	85.69	13.45	20.95	5.94	92.82	79.05	85.38
Ours No $\mathcal{L}_{\text{att}}$	6.89	9.44	4.35	83.78	90.56	87.03	5.82	10.38	1.26	81.31	89.62	85.26	14.61	21.24	7.98	90.56	78.76	84.25
Ours No $\mathcal{L}_{\text{dir}}$	7.50	10.69	4.31	83.70	89.31	86.42	4.97	8.49	1.45	79.41	91.51	85.03	15.26	21.62	8.90	89.54	78.38	83.59
Ours 2 iterations	6.63	9.30	3.96	85.02	90.70	87.77	5.41	9.73	1.09	83.50	90.27	86.75	13.22	20.68	5.77	93.03	79.32	85.63
Ours 3 iterations	6.50	7.92	5.09	81.75	92.08	86.61	5.04	8.72	1.36	80.34	91.28	85.46	12.92	16.37	9.48	89.55	83.63	86.49
Ours 5 iterations	6.11	7.23	4.99	82.15	92.77	87.14	5.83	10.46	1.20	81.93	89.54	85.57	13.51	17.97	9.05	89.80	82.03	85.74

Table 2: Inference time for different configurations of our framework compared to the retrained SILT model [67]. Inference times are reported in seconds per image.

Method	Inference (s)
SILT†	0.137
Ours Non-Iterative	0.176
Ours Iterative - 3 iters	0.545
Ours Iterative - 2 iters	0.347
Ours Iterative - 5 iters	0.894

Table 3: Quantitative results comparing the standalone light estimation module with the light estimation module integrated into our proposed framework.

Model	Light MAE
Standalone	0.034
Ours final 1st Iter.	0.061
Ours final 2nd Iter.	0.050
Ours final 3rd Iter.	0.049

2.4 Standalone Light Estimation Performance

To validate our light estimation strategy, we first evaluate a standalone light estimation module operating on ground-truth shadow masks. For SOBA and CUHK, heuristic light directions are used as pseudo ground truth, while WSRD [49] provides physically calibrated lighting. As a result, light-direction accuracy is quantitatively evaluated only on the 42 WSRD test images. Tab. 3 compares this standalone estimator with the light predictor used in our joint framework.

With ground-truth shadow masks, the standalone module achieves a light-direction MAE of 0.034, serving as an approximate upper-bound reference under our evaluation setting. When the light predictor is integrated into the iterative framework and driven by predicted shadows, the MAE is 0.061 at the first it-

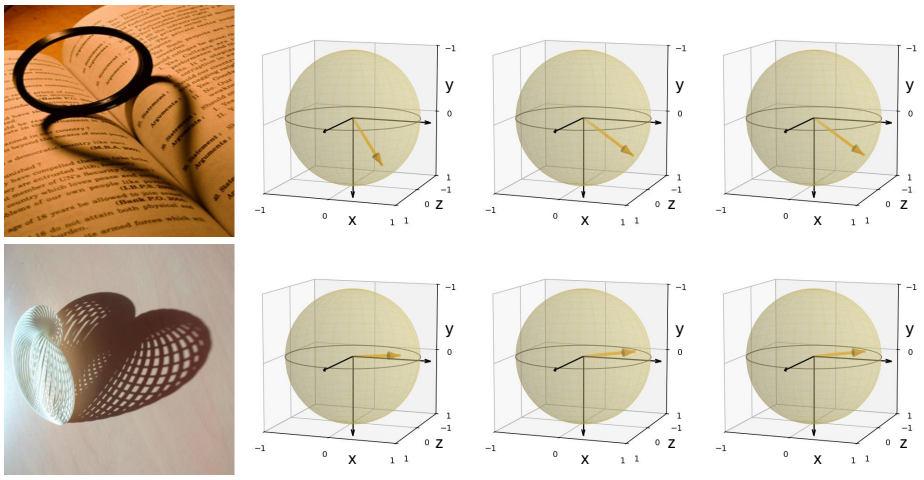


Fig. 8: Effectiveness of the iterative learning scheme. Our proposed feedback mechanism progressively refines the estimated light direction, with most of the improvement occurring by the second iteration and the results stabilizing at the third.

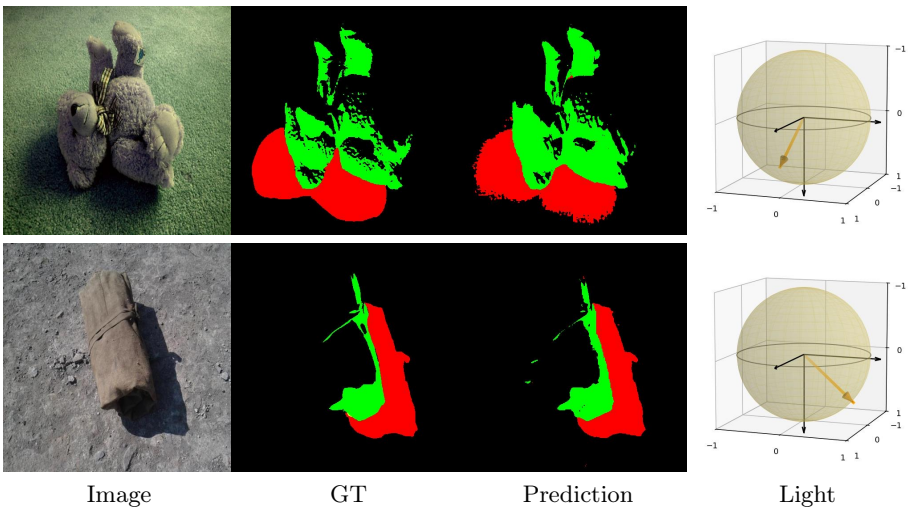


Fig. 9: Qualitative examples of cast and attached shadow predictions obtained using our estimated light directions.

eration and improves to 0.050 and 0.049 at the second and third iterations, respectively. This progressive reduction indicates that the iterative scheme refines the light estimates and steadily approaches the upper-bound performance, as illustrated in Fig. 8. Qualitative examples in Fig. 9 show that the predicted light directions are consistent with the observed cast and attached shadows.

3 Dataset

We introduce the first dataset curated specifically for the joint detection of *cast* and *attached* shadows. The dataset contains 1,166 training images and 292 test images. Each image is annotated with a normal map, light direction, object mask, cast-shadow mask, attached-shadow mask, and undefined-shadow mask.

Our proposed dataset is constructed from three existing sources: WSRD [49], SOBA [55], and CUHK [14]. These datasets were originally designed for different tasks: WSRD focuses on shadow removal with paired shadow/shadow-free images, SOBA provides instance-level cast-shadow annotations, and CUHK contains scene-level shadow masks. We unify and extend these annotations to support joint cast and attached shadow detection through the curation steps described below.

3.1 Cast and Attached Shadow Masks

SOBA. Cast shadow masks are provided in the official SOBA annotations [55]. To generate attached shadow masks, we first use the derived light direction and precomputed normal map to create a prior attached-shadow mask. Errors in this prior mask are then manually corrected to obtain high-quality attached shadow annotations. Examples of these manual corrections are shown in Fig. 10.

CUHK. CUHK provides full shadow masks for the scene; however, the quality of the attached shadow component in the provided annotations is not ideal, as attached shadows are not consistently labeled on object regions. Therefore, we manually correct the attached shadow masks for CUHK images. Examples of these corrections are shown in Fig. 11.



Fig. 10: Examples of manual corrections applied to attached shadows in SOBA images.



Fig. 11: Examples of manual corrections applied to attached shadows in CUHK images.

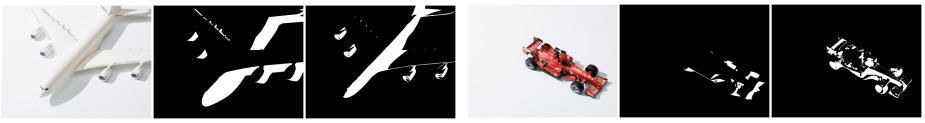


Fig. 12: Cast and attached shadow masks for WSRD images.

WSRD. For WSRD images, we obtain shadow masks by first performing color-based subtraction between the shadow and shadow-free images to identify regions with intensity changes. Next, we use the extracted object mask to differentiate between regions inside and outside the object, resulting in separate cast shadow masks and attached shadow masks, as illustrated in Fig. 12.

3.2 Depth Map

To enable reliable detection of attached shadows, accurate scene geometry is essential. Depth estimation, a fundamental task in computer vision [37, 39, 41, 42, 68], has recently demonstrated reliable performance on natural images. We use the off-the-shelf Depth Anything V2 [69] to extract relative depth maps from our images. The extracted depth maps are illustrated in Fig. 13 (second column).

3.3 Normal Map

Surface orientation plays a crucial role in determining attached shadows. To capture this, we extract normal maps from the depth maps. For each pixel, the third element (z-dimension) of the normal is set to 1, while the x and y components are given by the spatial gradients of the depth map. Surface normals are computed relative to the camera viewpoint, with the positive z-dimension pointing inward. The derived surface-normal maps are illustrated in Fig. 13 (third column).

3.4 Object Masks

For SOBA images, we directly use the object masks provided in the official annotations [55]. For WSRD and CUHK images, we use the state-of-the-art dichotomous image-segmentation model BiRefNet [73] to automatically extract object masks from the input images. These masks are used solely to define object-level annotations and for quantitative evaluation; they are not required by our method at test time. Fig. 14 shows representative examples of the extracted object masks for the WSRD and CUHK images.

3.5 Light Direction

Light direction is essential for identifying attached shadows.



Fig. 13: Geometric information. We first extract depth maps using [69] and then derive the corresponding surface-normal maps relative to the camera viewpoint.

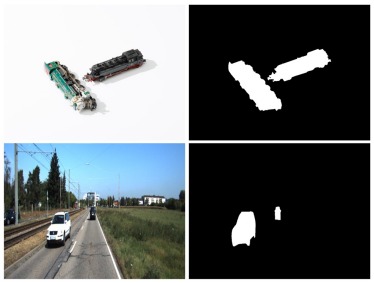


Fig. 14: Extracted object masks for WSRD and CUHK images.

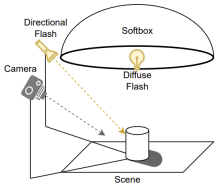


Fig. 15: WSRD data-acquisition setup. The camera is positioned at a 45-degree vertical angle toward the scene. A directional light source is mounted at a 45-degree vertical angle toward the scene and at a 90-degree horizontal angle relative to the camera. Image adapted from [48].

For WSRD images, the calibrated acquisition setup (Fig. 15) provides known camera and light-source positions. Using the provided angles, we compute a 3D light-direction vector and express it in a camera-centric coordinate system ($+x$ right, $+y$ down, $+z$ inward).

For SOBA and CUHK images, where calibration is unavailable, we estimate light direction from object–shadow pairs and depth. We first compute a 2D direction by connecting the centroid of an object to the centroid of its cast shadow, giving (v_x, v_y). We then compute the average depth difference Δd between object and shadow regions. The vector $(v_x, v_y, \Delta d)$ is normalized to obtain the light direction. When multiple object–shadow pairs exist, the resulting vectors are averaged to obtain a single direction for each image. The estimated light directions are illustrated in Fig. 16.

3.6 Undefined Shadow Masks

Our annotations focus on shadows associated with foreground objects. Shadow pixels that cannot be **reliably** attributed to these objects are labeled as *undefined shadows*.

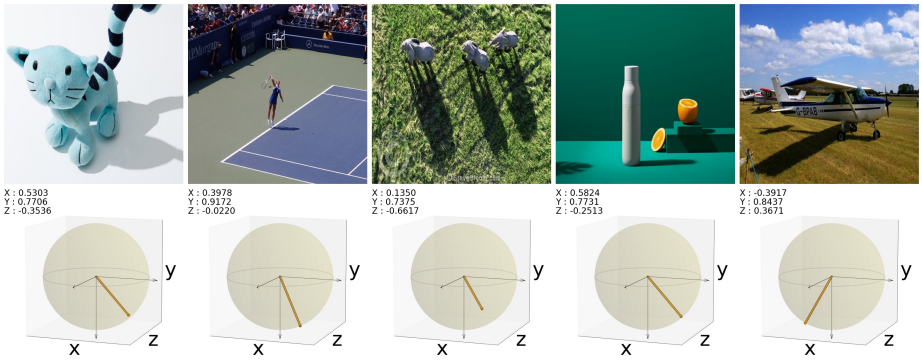


Fig. 16: Derived light directions for WSRD, SOBA, and CUHK images, expressed in the camera-centric coordinate system. The x, y, and z components of the unit light vectors are plotted.

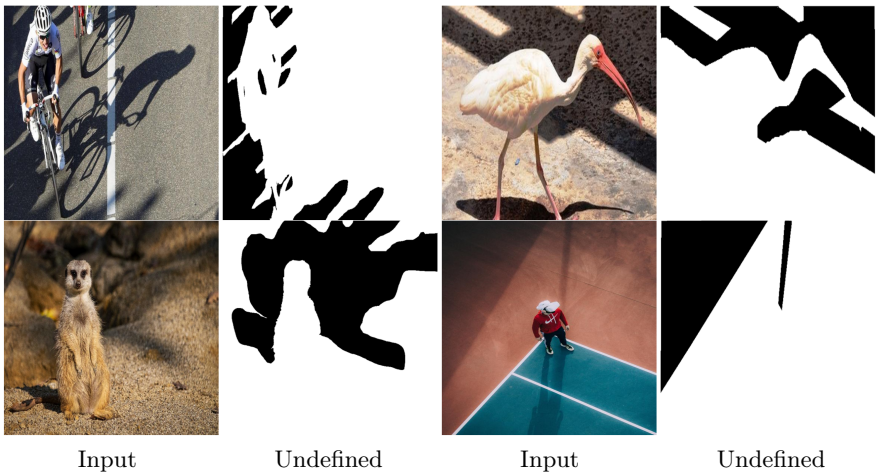


Fig. 17: Illustration of excluding undefined shadow regions when training and evaluating cast- and attached-shadow predictions on our dataset. Undefined shadow masks are used only for training and evaluation of full-shadow predictions.

For SOBA and CUHK images, we start from the provided scene-level shadow masks and mark regions not linked to annotated objects as undefined. These masks are used only for training and evaluation of full-shadow predictions. During cast/attached shadow training and evaluation, undefined regions are excluded (Fig. 17).

References

1. Bai, J., He, Z., Yang, S., Guo, J., Chen, Z., Zhang, Y., Guo, Y.: Local-to-global panorama inpainting for locale-aware indoor lighting prediction. IEEE Trans. Vis. Comput. Graph. **29**(11), 4405–4416 (2023). https://doi.org/10.1109/TVCG.2023.3320233
2. Chen, T., Zhu, L., Ding, C., Cao, R., Wang, Y., Zhang, S., Li, Z., Sun, L., Zang, Y., Mao, P.: SAM-adapter: Adapting segment anything in underperformed scenes. In: Proc. IEEE/CVF Int. Conf. Comput. Vis. Workshops (ICCVW). pp. 3359–3367 (2023). https://doi.org/10.1109/ICCVW60793.2023.00361
3. Chen, Z., Wan, L., Zhu, L., Shen, J., Fu, H., Liu, W., Qin, J.: Triple-cooperative video shadow detection. In: Proc. IEEE/CVF Conf. Comput. Vis. Pattern Recog. (CVPR). pp. 2714–2723 (2021). https://doi.org/10.1109/CVPR46437.2021.00274
4. Chen, Z., Zhu, L., Wan, L., Wang, S., Feng, W., Heng, P.A.: A multi-task mean teacher for semi-supervised shadow detection. In: Proc. IEEE/CVF Conf. Comput. Vis. Pattern Recog. (CVPR). pp. 5610–5619 (2020). https://doi.org/10.1109/CVPR42600.2020.00565
5. Chuang, Y.Y., Goldman, D.B., Curless, B., Salesin, D.H., Szeliski, R.: Shadow matting and compositing. ACM Trans. Graph. **22**(3), 494–500 (2003). https://doi.org/10.1145/1201775.882298
6. Cun, X., Pun, C.M., Shi, C.: Towards ghost-free shadow removal via dual hierarchical aggregation network and shadow matting GAN. In: Proc. AAAI Conf. Artif. Intell. vol. 34, pp. 10680–10687 (2020). https://doi.org/10.1609/aaai.v34i07.6695
7. Dastjerdi, M.R.K., Eisenmann, J., Hold-Geoffroy, Y., Lalonde, J.F.: EverLight: Indoor-outdoor editable HDR lighting estimation. In: Proc. IEEE/CVF Int. Conf. Comput. Vis. (ICCV). pp. 7386–7395 (2023). https://doi.org/10.1109/ICCV51070.2023.00682
8. Ding, B., Long, C., Zhang, L., Xiao, C.: ARGAN: Attentive recurrent generative adversarial network for shadow detection and removal. In: Proc. IEEE/CVF Int. Conf. Comput. Vis. (ICCV). pp. 10212–10221 (2019). https://doi.org/10.1109/ICCV.2019.01031
9. Gardner, M.A., Hold-Geoffroy, Y., Sunkavalli, K., Gagné, C., Lalonde, J.F.: Deep parametric indoor lighting estimation. In: Proc. IEEE/CVF Int. Conf. Comput. Vis. (ICCV). pp. 7174–7182 (2019). https://doi.org/10.1109/ICCV.2019.00727
10. Guo, L., Huang, S., Liu, D., Cheng, H., Wen, B.: ShadowFormer: Global context helps shadow removal. In: Proc. AAAI Conf. Artif. Intell. vol. 37, pp. 710–718 (2023). https://doi.org/10.1609/aaai.v37i1.25148
11. Guo, L., Wang, C., Yang, W., Huang, S., Wang, Y., Pfister, H., Wen, B.: ShadowDiffusion: When degradation prior meets diffusion model for shadow removal. In: Proc. IEEE/CVF Conf. Comput. Vis. Pattern Recog. (CVPR). pp. 14049–14058 (2023). https://doi.org/10.1109/CVPR52729.2023.01350
12. Hu, S., Le, H., Athar, S., Das, S., Samaras, D.: Shadow removal refinement via material-consistent shadow edges. In: Proc. IEEE/CVF Winter Conf. Appl. Comput. Vis. (WACV). pp. 2631–2641 (2025). https://doi.org/10.1109/WACV61041.2025.00261
13. Hu, X., Jiang, Y., Fu, C.W., Heng, P.A.: Mask-ShadowGAN: Learning to remove shadows from unpaired data. In: Proc. IEEE/CVF Int. Conf. Comput. Vis. (ICCV). pp. 2472–2481 (2019). https://doi.org/10.1109/ICCV.2019.00256

14. Hu, X., Wang, T., Fu, C.W., Jiang, Y., Wang, Q., Heng, P.A.: Revisiting shadow detection: A new benchmark dataset for complex world. IEEE Trans. Image Process. **30**, 1925–1934 (2021). https://doi.org/10.1109/TIP.2021.3049331
15. Hu, X., Zhu, L., Fu, C.W., Qin, J., Heng, P.A.: Direction-aware spatial context features for shadow detection. In: Proc. IEEE/CVF Conf. Comput. Vis. Pattern Recog. (CVPR). pp. 7454–7462 (2018). https://doi.org/10.1109/CVPR.2018.00778
16. Jin, Y., Ye, W., Yang, W., Yuan, Y., Tan, R.T.: DeS3: Adaptive attention-driven self and soft shadow removal using ViT similarity. In: Proc. AAAI Conf. Artif. Intell. vol. 38, pp. 2634–2642 (2024). https://doi.org/10.1609/aaai.v38i3.28041
17. KaewTraKulPong, P., Bowden, R.: An improved adaptive background mixture model for real-time tracking with shadow detection. In: Video-Based Surveillance Systems, pp. 135–144. Springer (2002). https://doi.org/10.1007/978-1-4615-0913-4_11
18. Kingma, D.P., Ba, J.: Adam: A method for stochastic optimization (2017). https://doi.org/10.48550/arXiv.1412.6980
19. Lalonde, J.F., Efros, A.A., Narasimhan, S.G.: Detecting ground shadows in outdoor consumer photographs. In: Proc. Eur. Conf. Comput. Vis. (ECCV). pp. 322–335 (2010). https://doi.org/10.1007/978-3-642-15552-9_24
20. Le, H., Nguyen, V., Yu, C.P., Samaras, D.: Geodesic distance histogram feature for video segmentation. In: Proc. Asian Conf. Comput. Vis. (ACCV). pp. 275–290 (2016). https://doi.org/10.1007/978-3-319-54181-5_18
21. Le, H., Samaras, D.: Shadow removal via shadow image decomposition. In: Proc. IEEE/CVF Int. Conf. Comput. Vis. (ICCV). pp. 8577–8586 (2019). https://doi.org/10.1109/ICCV.2019.00867
22. Le, H., Samaras, D.: From shadow segmentation to shadow removal. In: Proc. Eur. Conf. Comput. Vis. (ECCV). pp. 264–281 (2020). https://doi.org/10.1007/978-3-030-58621-8_16
23. Le, H., Samaras, D.: Physics-based shadow image decomposition for shadow removal. IEEE Trans. Pattern Anal. Mach. Intell. **44**(12), 9088–9101 (2022). https://doi.org/10.1109/TPAMI.2021.3124934
24. Le, H., Samaras, D., Lynch, H.J.: A convolutional neural network architecture designed for the automated survey of seabird colonies. Remote Sens. Ecol. Conserv. **8**(2), 251–262 (2022). https://doi.org/10.1002/rse2.240
25. Le, H., Vicente, T.F.Y., Nguyen, V., Hoai, M., Samaras, D.: A+D Net: Training a shadow detector with adversarial shadow attenuation. In: Proc. Eur. Conf. Comput. Vis. (ECCV). pp. 680–696 (2018). https://doi.org/10.1007/978-3-030-01216-8_41
26. Le, H., Yu, C.P., Zelinsky, G., Samaras, D.: Co-localization with category-consistent features and geodesic distance propagation. In: Proc. IEEE Int. Conf. Comput. Vis. Workshops (ICCVW). pp. 1103–1112 (2017). https://doi.org/10.1109/ICCVW.2017.134
27. Le, H.M., Goncalves, B., Samaras, D., Lynch, H.: Weakly labeling the antarctic: The penguin colony case. In: Proc. IEEE/CVF Conf. Comput. Vis. Pattern Recog. Workshops (CVPRW). pp. 18–25 (2019). https://doi.org/10.48550/arXiv.1905.03313
28. Li, X., Guo, Q., Abdelfattah, R., Lin, D., Feng, W., Tsang, I., Wang, S.: Leveraging inpainting for single-image shadow removal. In: Proc. IEEE/CVF Int. Conf. Comput. Vis. (ICCV). pp. 13009–13018 (2023). https://doi.org/10.1109/ICCV51070.2023.01200

29. Liu, Z., Mao, H., Wu, C.Y., Feichtenhofer, C., Darrell, T., Xie, S.: A ConvNet for the 2020s. In: Proc. IEEE/CVF Conf. Comput. Vis. Pattern Recog. (CVPR). pp. 11966–11976 (2022). https://doi.org/10.1109/CVPR52688.2022.01167
30. Okabe, T., Sato, I., Sato, Y.: Attached shadow coding: Estimating surface normals from shadows under unknown reflectance and lighting conditions. In: Proc. IEEE Int. Conf. Comput. Vis. (ICCV). pp. 1693–1700 (2009). https://doi.org/10.1109/ICCV.2009.5459381
31. Panagopoulos, A., Samaras, D., Paragios, N.: Robust shadow and illumination estimation using a mixture model. In: Proc. IEEE Conf. Comput. Vis. Pattern Recog. Workshops (CVPRW) (2009). https://doi.org/10.1109/CVPRW.2009.5206665
32. Panagopoulos, A., Vicente, T.F.Y., Samaras, D.: Illumination estimation from shadow borders. In: Proc. IEEE Int. Conf. Comput. Vis. Workshops (ICCVW). pp. 798–805 (2011). https://doi.org/10.1109/ICCVW.2011.6130334
33. Panagopoulos, A., Wang, C., Samaras, D., Paragios, N.: Illumination estimation and cast shadow detection through a higher-order graphical model. In: Proc. IEEE Conf. Comput. Vis. Pattern Recog. (CVPR). pp. 673–680 (2011). https://doi.org/10.1109/CVPR.2011.5995585
34. Panagopoulos, A., Wang, C., Samaras, D., Paragios, N.: Estimating shadows with the bright channel cue. In: Trends and Topics in Computer Vision. pp. 1–12 (2012). https://doi.org/10.1007/978-3-642-35740-4_1
35. Panagopoulos, A., Wang, C., Samaras, D., Paragios, N.: Simultaneous cast shadows, illumination and geometry inference using hypergraphs. IEEE Trans. Pattern Anal. Mach. Intell. **35**(2), 437–449 (2013). https://doi.org/10.1109/TPAMI.2012.110
36. Paszke, A., Gross, S., Massa, F., Lerer, A., Bradbury, J., Chanan, G., Killeen, T., Lin, Z., Gimelshein, N., Antiga, L., Desmaison, A., Köpf, A., Yang, E., DeVito, Z., Raison, M., Tejani, A., Chilamkurthy, S., Steiner, B., Fang, L., Bai, J., Chintala, S.: PyTorch: An imperative style, high-performance deep learning library. In: Adv. Neural Inf. Process. Syst. (NeurIPS). vol. 32 (2019). https://doi.org/10.48550/arXiv.1912.01703
37. Patni, S., Agarwal, A., Arora, C.: ECoDepth: Effective conditioning of diffusion models for monocular depth estimation. In: Proc. IEEE/CVF Conf. Comput. Vis. Pattern Recog. (CVPR). pp. 28285–28295 (2024). https://doi.org/10.1109/CVPR52733.2024.02672
38. Phongthawee, P., Chinchuthakun, W., Sinsunthithet, N., Jampani, V., Raj, A., Khungurn, P., Suwajanakorn, S.: DiffusionLight: Light probes for free by painting a chrome ball. In: Proc. IEEE/CVF Conf. Comput. Vis. Pattern Recog. (CVPR). pp. 98–108 (2024). https://doi.org/10.1109/CVPR52733.2024.00018
39. Piccinelli, L., Yang, Y.H., Sakaridis, C., Segu, M., Li, S., Gool, L.V., Yu, F.: UniDepth: Universal monocular metric depth estimation. In: Proc. IEEE/CVF Conf. Comput. Vis. Pattern Recog. (CVPR). pp. 10106–10116 (2024). https://doi.org/10.1109/CVPR52733.2024.00963
40. Qu, L., Tian, J., He, S., Tang, Y., Lau, R.W.H.: DeshadowNet: A multi-context embedding deep network for shadow removal. In: Proc. IEEE Conf. Comput. Vis. Pattern Recog. (CVPR). pp. 2308–2316 (2017). https://doi.org/10.1109/CVPR.2017.248
41. Ranftl, R., Bochkovskiy, A., Koltun, V.: Vision transformers for dense prediction. In: Proc. IEEE/CVF Int. Conf. Comput. Vis. (ICCV). pp. 12159–12168 (2021). https://doi.org/10.1109/ICCV48922.2021.01196

42. Ranftl, R., Lasinger, K., Hafner, D., Schindler, K., Koltun, V.: Towards robust monocular depth estimation: Mixing datasets for zero-shot cross-dataset transfer. IEEE Trans. Pattern Anal. Mach. Intell. **44**(3), 1623–1637 (2022). https://doi.org/10.1109/TPAMI.2020.3019967
43. Sato, I., Sato, Y., Ikeuchi, K.: Illumination from shadows. IEEE Trans. Pattern Anal. Mach. Intell. **25**(3), 290–300 (2003). https://doi.org/10.1109/TPAMI.2003.1182093
44. Somanath, G., Kurz, D.: HDR environment map estimation for real-time augmented reality. In: Proc. IEEE/CVF Conf. Comput. Vis. Pattern Recog. (CVPR). pp. 11293–11301 (2021). https://doi.org/10.1109/CVPR46437.2021.01114
45. Sudre, C.H., Li, W., Vercauteren, T., Ourselin, S., Cardoso, M.J.: Generalised dice overlap as a deep learning loss function for highly unbalanced segmentations. In: Proc. Deep Learn. Med. Image Anal. Multimodal Learn. Clin. Decis. Support. pp. 240–248 (2017). https://doi.org/10.1007/978-3-319-67558-9_28
46. Sun, J., Xu, K., Pang, Y., Zhang, L., Lu, H., Hancke, G., Lau, R.: Adaptive illumination mapping for shadow detection in raw images. In: Proc. IEEE/CVF Int. Conf. Comput. Vis. (ICCV). pp. 12663–12672 (2023). https://doi.org/10.1109/ICCV51070.2023.01167
47. Sunkavalli, K., Zickler, T., Pfister, H.: Visibility subspaces: Uncalibrated photometric stereo with shadows. In: Proc. Eur. Conf. Comput. Vis. (ECCV). pp. 251–264 (2010). https://doi.org/10.1007/978-3-642-15552-9_19
48. Vasluianu, F.A., Seizinger, T., Timofte, R.: WSRD: A novel benchmark for high resolution image shadow removal. In: Proc. IEEE/CVF Conf. Comput. Vis. Pattern Recog. Workshops (CVPRW). pp. 1826–1835 (2023). https://doi.org/10.1109/CVPRW59228.2023.00181
49. Vasluianu, F.A., Seizinger, T., Zhou, Z., Wu, Z., Chen, C., Timofte, R., et al.: NTIRE 2024 image shadow removal challenge report. In: Proc. IEEE/CVF Conf. Comput. Vis. Pattern Recog. Workshops (CVPRW). pp. 6547–6570 (2024). https://doi.org/10.1109/CVPRW63382.2024.00654
50. Verbin, D., Mildenhall, B., Hedman, P., Barron, J.T., Zickler, T., Srinivasan, P.P.: Eclipse: Disambiguating illumination and materials using unintended shadows. In: Proc. IEEE/CVF Conf. Comput. Vis. Pattern Recog. (CVPR). pp. 77–86 (2024). https://doi.org/10.1109/CVPR52733.2024.00016
51. Vicente, T.F.Y., Hou, L., Yu, C.P., Hoai, M., Samaras, D.: Large-scale training of shadow detectors with noisily-annotated shadow examples. In: Proc. Eur. Conf. Comput. Vis. (ECCV). pp. 816–832 (2016). https://doi.org/10.1007/978-3-319-46466-4_49
52. Wang, J., Li, X., Yang, J.: Stacked conditional generative adversarial networks for jointly learning shadow detection and shadow removal. In: Proc. IEEE/CVF Conf. Comput. Vis. Pattern Recog. (CVPR). pp. 1788–1797 (2018). https://doi.org/10.1109/CVPR.2018.00192
53. Wang, T., Hu, X., Fu, C.W., Heng, P.A.: Single-stage instance shadow detection with bidirectional relation learning. In: Proc. IEEE/CVF Conf. Comput. Vis. Pattern Recog. (CVPR). pp. 1–11 (2021). https://doi.org/10.1109/CVPR46437.2021.00007
54. Wang, T., Hu, X., Heng, P.A., Fu, C.W.: Instance shadow detection with a single-stage detector. IEEE Trans. Pattern Anal. Mach. Intell. **45**(3), 3259–3273 (2023). https://doi.org/10.1109/TPAMI.2022.3185628
55. Wang, T., Hu, X., Wang, Q., Heng, P.A., Fu, C.W.: Instance shadow detection. In: Proc. IEEE/CVF Conf. Comput. Vis. Pattern Recog. (CVPR). pp. 1877–1886 (2020). https://doi.org/10.1109/CVPR42600.2020.00195

56. Wang, T., Zhang, J., Zheng, H., Ding, Z., Cohen, S., Lin, Z., Xiong, W., Fu, C.W., Figueroa, L., Kim, S.Y.: MetaShadow: Object-centered shadow detection, removal, and synthesis. In: Proc. IEEE/CVF Conf. Comput. Vis. Pattern Recog. (CVPR). pp. 28252–28262 (2025). https://doi.org/10.1109/CVPR52734.2025.02631
57. Wang, W., Xie, E., Li, X., Fan, D.P., Song, K., Liang, D., Lu, T., Luo, P., Shao, L.: PVT v2: Improved baselines with pyramid vision transformer. Comput. Vis. Media **8**(3), 415–424 (2022). https://doi.org/10.1007/s41095-022-0274-8
58. Wang, Y., Curless, B.L., Seitz, S.M.: People as scene probes. In: Proc. Eur. Conf. Comput. Vis. (ECCV). pp. 438–454 (2020). https://doi.org/10.1007/978-3-030-58607-2_26
59. Wang, Y., Liu, S., Li, L., Zhou, W., Li, H.: SwinShadow: Shifted window for ambiguous adjacent shadow detection. ACM Trans. Multimedia Comput. Commun. Appl. **20**(11), 1–20 (2024). https://doi.org/10.1145/3688803
60. Wu, H., Xu, J., Le, H., Samaras, D.: Importance-based token merging for efficient image and video generation. In: Proc. IEEE/CVF Int. Conf. Comput. Vis. (ICCV). pp. 4983–4995 (2025). https://doi.org/10.1109/ICCV51701.2025.00474
61. Xing, Z., Wang, T., Hu, X., Wu, H., Fu, C.W., Heng, P.A.: Video instance shadow detection under the sun and sky. IEEE Trans. Image Process. **33**, 5715–5726 (2024). https://doi.org/10.1109/TIP.2024.3468877
62. Xu, J., Le, H.: Generating representative samples for few-shot classification. In: Proc. IEEE/CVF Conf. Comput. Vis. Pattern Recog. (CVPR). pp. 8993–9003 (2022). https://doi.org/10.1109/CVPR52688.2022.00880
63. Xu, J., Le, H., Huang, M., Athar, S., Samaras, D.: Variational feature disentangling for fine-grained few-shot classification. In: Proc. IEEE/CVF Int. Conf. Comput. Vis. (ICCV). pp. 8792–8801 (2021). https://doi.org/10.1109/ICCV48922.2021.00869
64. Xu, J., Le, H., Nguyen, V., Ranjan, V., Samaras, D.: Zero-shot object counting. In: Proc. IEEE/CVF Conf. Comput. Vis. Pattern Recog. (CVPR). pp. 15548–15557 (2023). https://doi.org/10.1109/CVPR52729.2023.01492
65. Xu, J., Le, H., Samaras, D.: Generating features with increased crop-related diversity for few-shot object detection. In: Proc. IEEE/CVF Conf. Comput. Vis. Pattern Recog. (CVPR). pp. 19713–19722 (2023). https://doi.org/10.1109/CVPR52729.2023.01888
66. Xu, J., Le, H., Samaras, D.: Assessing sample quality via the latent space of generative models. In: Proc. Eur. Conf. Comput. Vis. (ECCV). pp. 449–464 (2024). https://doi.org/10.1007/978-3-031-73202-7_26
67. Yang, H., Wang, T., Hu, X., Fu, C.W.: SILT: Shadow-aware iterative label tuning for learning to detect shadows from noisy labels. In: Proc. IEEE/CVF Int. Conf. Comput. Vis. (ICCV). pp. 12641–12652 (2023). https://doi.org/10.1109/ICCV51070.2023.01165
68. Yang, L., Kang, B., Huang, Z., Xu, X., Feng, J., Zhao, H.: Depth anything: Unleashing the power of large-scale unlabeled data. In: Proc. IEEE/CVF Conf. Comput. Vis. Pattern Recog. (CVPR). pp. 10371–10381 (2024). https://doi.org/10.1109/CVPR52733.2024.00987
69. Yang, L., Kang, B., Huang, Z., Zhao, Z., Xu, X., Feng, J., Zhao, H.: Depth anything V2. In: Adv. Neural Inf. Process. Syst. (NeurIPS). vol. 37, pp. 21875–21911 (2024). https://doi.org/10.52202/079017-0688
70. Yang, Y., Hu, S., Wu, H., Baldrich, R., Samaras, D., Vanrell, M.: mli-NeRF: Multi-light intrinsic-aware neural radiance fields. In: Proc. Int. Conf. 3D Vision (3DV). pp. 587–596 (2025). https://doi.org/10.1109/3DV66043.2025.00059

71. Zhang, J., Sunkavalli, K., Hold-Geoffroy, Y., Hadap, S., Eisenman, J., Lalonde, J.F.: All-weather deep outdoor lighting estimation. In: Proc. IEEE/CVF Conf. Comput. Vis. Pattern Recog. (CVPR). pp. 10150–10158 (2019). https://doi.org/10.1109/CVPR.2019.01040
72. Zhang, W., Zhao, X., Morvan, J.M., Chen, L.: Improving shadow suppression for illumination robust face recognition. IEEE Trans. Pattern Anal. Mach. Intell. **41**(3), 611–624 (2019). https://doi.org/10.1109/TPAMI.2018.2803179
73. Zheng, P., Gao, D., Fan, D.P., Liu, L., Laaksonen, J., Ouyang, W., Sebe, N.: Bilateral reference for high-resolution dichotomous image segmentation. CAAI Artif. Intell. Res. p. 9150038 (2024). https://doi.org/10.26599/AIR.2024.9150038
74. Zheng, Q., Qiao, X., Cao, Y., Lau, R.W.H.: Distraction-aware shadow detection. In: Proc. IEEE/CVF Conf. Comput. Vis. Pattern Recog. (CVPR). pp. 5162–5171 (2019). https://doi.org/10.1109/CVPR.2019.00531
75. Zhu, L., Deng, Z., Hu, X., Fu, C.W., Xu, X., Qin, J., Heng, P.A.: Bidirectional feature pyramid network with recurrent attention residual modules for shadow detection. In: Proc. Eur. Conf. Comput. Vis. (ECCV). pp. 122–137 (2018). https://doi.org/10.1007/978-3-030-01231-1_8
76. Zhu, L., Xu, K., Ke, Z., Lau, R.W.H.: Mitigating intensity bias in shadow detection via feature decomposition and reweighting. In: Proc. IEEE/CVF Int. Conf. Comput. Vis. (ICCV). pp. 4682–4691 (2021). https://doi.org/10.1109/ICCV48922.2021.00466
77. Zhu, Y., Fu, X., Cao, C., Wang, X., Sun, Q., Zha, Z.J.: Single image shadow detection via complementary mechanism. In: Proc. ACM Int. Conf. Multimedia (ACM MM). pp. 6717–6726 (2022). https://doi.org/10.1145/3503161.3547904
78. Zhu, Z., Woodcock, C.E.: Object-based cloud and cloud shadow detection in Landsat imagery. Remote Sens. Environ. **118**, 83–94 (2012). https://doi.org/10.1016/j.rse.2011.10.028